energies

MDPI

Article

Underbody Impacts on EV Power Battery Packs: Modeling of Macromechanical and Internal Effects

Zhijie Li [1,*], Liejun Li [2], Yuchao Wang [1], Jiqing Chen [2] and Fengchong Lan [2]

[1] Guangzhou Automobile Group Corporation, Guangzhou 526040, China; wangyuchao10@gac.com.cn
[2] School of Mechanical and Automotive Engineering, South China University of Technology, Guangzhou 510641, China; liliejun@scut.edu.cn (L.L.); chjq@scut.edu.cn (J.C.); fclan@scut.edu.cn (F.L.)
* Correspondence: heaton_lzj@163.com; Tel.: +86-18814124387

Abstract

Short circuits and subsequent fires resulting from objects impacting the bottom of vehicle power battery packs considerably jeopardize electric vehicle (EV) operations. This study investigated underbody impacts in EVs and the overall mechanical properties of battery cells. Key features of road debris were extracted and simplified to establish a geometric parameter structure model and determine realistic battery pack responses to debris impact. Quasi-static compression and dynamic impact tests on a prismatic lithium-ion battery (LIB) and power battery pack followed. Macroscopic mechanical responses, deformation failure modes, and internal jellyroll damage of cells and packs were evaluated, and constitutive equations and failure parameters were derived to develop a finite element model, whose effectiveness and reliability were verified by comparing simulation results with experimental data. Finally, a homogenized model of the prismatic LIB and power battery pack was constructed, which effectively predicted the macroscopic mechanical response and internal short-circuit failure under mechanical loading. However, simulation and test results revealed certain deviations in cell indentations under battery pack bottom impacts, presumably because the FEMs neglect the dynamic strain rate effects of electrolyte and cooling liquid. Overall, this study elucidates safety risks to cells and their key components under power battery pack bottom impacts.

Keywords: electric vehicle; vehicle power battery pack; lithium-ion battery; battery cell; road debris impact; dynamic impact test; finite element model

Check for updates

Academic Editor: King Jet Tseng

Received: 20 April 2026
Revised: 15 May 2026
Accepted: 19 May 2026
Published: 12 June 2026

Copyright: © 2026 by the authors. Licensee MDPI, Basel, Switzerland. This article is an open access article distributed under the terms and conditions of the Creative Commons Attribution (CC BY) license.

1. Introduction

The protection of lithium-ion batteries (LIBs) from impact-related damage is a major concern for automotive manufacturers. Because battery packs of electric vehicles (EVs) contain a large number of highly integrated cells, they are typically positioned underneath the vehicle. Although this design significantly improves the comfort and space of the passenger compartment, it reduces the ground clearance of the vehicle. Reduced ground clearance increases the risk of road debris intruding into the bottom of the battery pack, potentially leading to serious fire accidents [1]. Several high-profile accidents have been reported in which EVs ignited following underbody impacts; for example, a BYD EV taxi in Haikou City, Hainan Province, on 9 October 2021; a Tesla Model S in Shenzhen on 17 February 2023; an XPENG P7 in Shaoxing, Zhejiang, on 31 October 2023; a LEAPMOTOR C11 in Zhaoqing, Guangdong, on 11 April 2024; and a ZEEKR 009 in Baoshan, Yunnan, on 26 November 2024. Underbody scraping and the impact of external objects are the primary

factors contributing to fire accidents in EVs. Therefore, conducting safety research on the bottom parts of power battery packs is important for improving EV safety.

Existing literature mainly focuses on enhancing the impact resistance of the protective structures of EVs and reducing the deformation of battery cells. For example, Xia et al. [2] developed an approach suitable for analyzing impacts to battery pack bottoms, studying the process of foreign objects on the road impacting EV battery packs across multiple scales, including cell, module, and pack levels. They elucidated the protective mechanisms of various structural components of battery packs, such as the bottom protective plates, floors, crossbeams, and side rails, providing guidance for anti-impact designs of battery packs. Rawlinson and Clarke et al. [3] developed a side-impact vehicle energy absorption and distribution system incorporating the battery pack shell, including the bottom protective plate of the battery pack. A double-layered protective plate and foam–panel core sandwich structure composed of aluminum alloy, foam aluminum, and steel was recommended to improve the impact resistance of the battery pack. Subsequently, building on the research of Xia and Rawlinson, Zhu and Zhang [4] proposed four battery pack structure designs—involving three reinforced protective plates and one reinforced outer shell box—to evaluate the protective performance of battery packs. The results showed that the "BRAS" structure design most effectively reduced battery cell deformation, preventing buckling and providing stable resistance, thereby improving the impact resistance of the battery pack structure. Several key issues regarding research on bottom impacts to power battery packs require further investigation. First, safety standards for battery pack bottom compression strength and impact resistance have not yet been formally implemented. Second, relevant research on EV underbody impact by external objects remains lacking compared to the frontal and side collision scenarios required for crash safety tests. Moreover, structural crashworthiness research on battery packs has focused more on optimizing the designs of the body frame and battery-pack mounting lugs [5–7]. Finally, during the assembly of battery systems, LIB cells are often stacked vertically to form modules. This vertical arrangement indicates that during a bottom impact, primary deformation occurs along the vertical direction. However, most studies on the mechanical integrity of LIB cells have focused on large (in-plane) compression and three-point bending [8–10]. Furthermore, no refined finite element model (FEM) of a vehicle power battery pack has yet been applied to compare simulation results with actual test conditions. Therefore, it is necessary to conduct relevant research to address the aforementioned issues.

In this study, the key features of road debris were simplified and extracted from an in-depth analysis of road debris safety accident data, leading to the establishment of a geometric parameter structure model for road debris and the selection of an appropriate load type for bottom impact with hard objects. Next, quasi-static and dynamic tests and data analyses were performed on industry-standard prismatic LIBs and a power battery pack to observe and evaluate the deformation response of the cells and battery pack before and after testing. Finally, a homogenized model of the LIB and power battery pack was constructed. The reliability and effectiveness of the modeling method were verified by comparing simulation and experimental results, and the deformation response of the key components of the battery pack under the bottom impact load was evaluated.

2. Methodology

The specific process of the research method is as follows:

(1) Geometric modeling of road foreign objects and bottom-impact analysis, which lays the foundation for the subsequent finite element simulation analysis of the bottom impact of the power battery pack in terms of loading conditions.

(2) Quasi-static compression and dynamic impact tests were conducted on prismatic LIB cells and their battery packs to provide experimental data for validating the reliability of the methods adopted for developing FEMs.
(3) A homogenized FEM for an individual prismatic LIB cell and a refined FEM for bottom ball impacts on the power battery pack were developed.

3. Analysis of Road Debris in Power Battery Pack Bottom-Impact Accidents

3.1. Analysis of Impact Deformation Damage at the Bottom of Power Battery Packs

Sharp objects can easily pierce the bottom structural components of EV underbody battery packs, damaging internal structures such as the floor, mounting brackets, and battery modules. Although blunt objects cannot easily pierce the bottom structural components, they produce a larger deformation area. This reduces the overall strength of the underbody structure and may cause cell deformation, resulting in potential safety hazards. To better predict the structural damage response of the battery pack under impact, it is necessary to study the geometric structure of road debris. However, the number of investigation reports revealing the relationship between road debris and vehicle damage is limited. Fortunately, the US National Automotive Sampling System Crashworthiness Data System (NASS-CDS) provides data on vehicle underbody damage during impacts. This enabled an indirect study of the relationship between road debris and impact damage through vehicle-damage records. The National Highway Traffic Safety Administration (NHTSA) is the primary source of traffic crash data in the United States, covering fatalities, injuries, causative factors, vehicle damage, occupant conditions (crashworthiness), and safety program evaluations. It provides nationally representative vehicle damage and occupant condition data that form the foundation of a damage database [11].

According to the contact area between road debris and the vehicle underbody, damage can be divided into three categories, as shown in Figure 1. The red dashed line represents the deformed area.

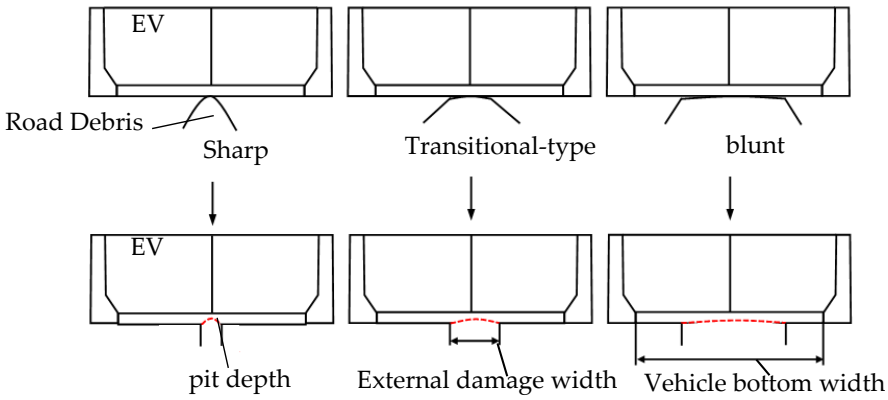

Figure 1. Deformation of and damage to electric vehicle (EV) underbody: front sectional view.

3.1.1. Damage from Sharp Road Debris

This type of road debris generally has a sharp edge, such as stones or metal objects with sharp-edged structures. The external damage width of the pit is minimal, whereas the penetration depth into the underbody is maximized. This indicates that sharp road debris has a small contact area with the vehicle underbody, and the resulting high strain concentration leads to underbody fracture at a relatively low penetration depth, causing further damage to adjacent structural components.

3.1.2. Damage from Transition-Type Road Debris

Contact with this type of road debris results in neither a sharp edge nor a large contact area. Transition-type road debris causes the most common type of destructive contact and is found among a wide variety of road debris types. The resulting damage pattern is intermediate between those of sharp and blunt debris types.

3.1.3. Damage from Blunt Road Debris

This type of road debris, which includes round stones and other rounded objects, generally has a large surface area. Blunt road debris has a large contact area with the vehicle underbody and causes overall deformation of the bottom structure. The penetration force is significantly smaller, making it comparatively difficult to puncture the vehicle underbody.

According to the statistics mentioned above, the form of underbody structural damage is closely related to the shape and size of the road debris. Using the two fundamental parameters of pit depth and external damage width/vehicle bottom width, the degree of damage caused by the geometric size of road foreign objects to the vehicle underbody structure can be evaluated. Under identical external impacts, the indentation depth follows the order: sharp road debris > transition-type road debris > blunt road debris. By contrast, the external damage width/vehicle underbody width follows the order: blunt road debris > transition-type road debris > sharp road debris. Overall, the geometric dimensions of road debris are closely associated with underbody damage and deformation, thus supporting the modeling principles of road debris discussed in the following sections.

3.2. Road Foreign Matter Collection and Data Analysis

The geometric characteristics of road debris are complex, diverse, and uncertain. These characteristics comprise multiple dimensions and elements, with primary attributes including shape, texture, and color. Considering the requirements for modeling the geometric features and deformability of road debris, as well as the variability of attributes such as color and texture, and given the close relationship between debris size and impact damage, geometric shape and size are the main research objects. An ideal method for extracting three-dimensional geometric features should satisfy at least three conditions: (1) simplicity and effectiveness: the feature extraction method should be simple and effective rather than overly complex; (2) concise representation with fidelity: the feature representation should be concise while ensuring that the main features of the geometric shape are accurately preserved; and (3) invariance and robustness: the features must possess invariance and strong robustness to ensure that the extracted features accurately reflect their attributes in subsequent modeling.

The crashworthiness analysis should accurately define the shape and impact form of the road debris and reasonably reproduce the impact scenario of road debris striking the underbody power battery pack. Considering the occurrence probability of road debris and the impact forms affecting the underbody power battery pack, two types of metal objects and curved stones were selected. To characterize the geometric characteristics of road stones, a four-step research approach was used: stone collection, screening and classification, measurement and recording, and data analysis.

3.2.1. Stone Collection

A number of road stone samples were collected from various roads. Although the collection frequency was not uniform across all roads, detailed information on the road stones was controlled to ensure random sampling. Subsequently, a road stone collection information Table 1, shown below, was prepared in advance to ensure the collection of all necessary information.

Table 1. Specific Descriptions of Foreign Objects on the Road.

Type	Ratio	Specific Description	Road Type	Road Photos
Stones	30%	Curbstones, obstruction stones, scattered stones	Mountain expressway	
Steel objects	30%	Metal pipes, metal rods, trailer hooks	Urban expressway	
Auto parts	30%	Tire fragments, driveshafts, bumpers, brake components		
Others	10%	Others		

3.2.2. Screening and Classification

After the stones were collected, they were screened and classified into two categories according to their outline size, represented by the maximum external sphere diameter D of the stones: 100–150 and 150–200 mm. Because of their size, these stones can collide with and contact the vehicle underbody, as shown in Figure 2.



100–150 mm 150–200 mm

(**a**) (**b**)

Figure 2. Screening and classification of road stones: (**a**) stones with sphere diameters of 100–150 mm; (**b**) stones with sphere diameters of 150–200 mm.

3.2.3. Dimension Measuring

After screening and classification, the road stones were measured. The measurement parameters included the maximum external sphere diameter, curvature radius of the curved surface, and tip angle of the road stones. The specific measurement steps and requirements are as follows.

The maximum external sphere diameter, D, of a stone was used to represent the outline size of the road debris. The measurement procedure was as follows. The stone was placed between the ground and a measuring ruler. By placing, rotating, and moving the stone in various orientations, the distance between the measuring ruler and the ground was maximized. This dimension was defined as the maximum external sphere diameter, D, as shown in Figure 3a.

The radius of surface curvature ρ reflects the shape of the stone surface and is an important parameter for describing the shape of a 3D model. The larger the curvature radius, the smaller the degree of bending, suggesting a flatter stone surface. Because many curved surfaces can be identified on a stone surface, it is not practical to measure each one individually. Therefore, three to five main characteristics were randomly selected for measurement. The minimum and maximum radii of curvature were recorded as $\rho_{n/min}$ and $\rho_{n/max}$, where n is the label number of the stone and m is the measurement sequence of a single stone, and n and m are positive integers, as shown in Figure 3b. The tip angle β represents the sharpness or bluntness of the stone. The smaller the tip angle, the sharper the stone, and vice versa. Because numerous tip angles may appear on a stone, three to five randomly selected tips were used to measure β. The minimum and maximum tip angles were selected and recorded as $\beta_{n/min}$ and $\beta_{n/max}$, respectively, where n is the serial

number of the stone and m is the measurement sequence for a single stone; both n and m are positive integers, as shown in Figure 3c.

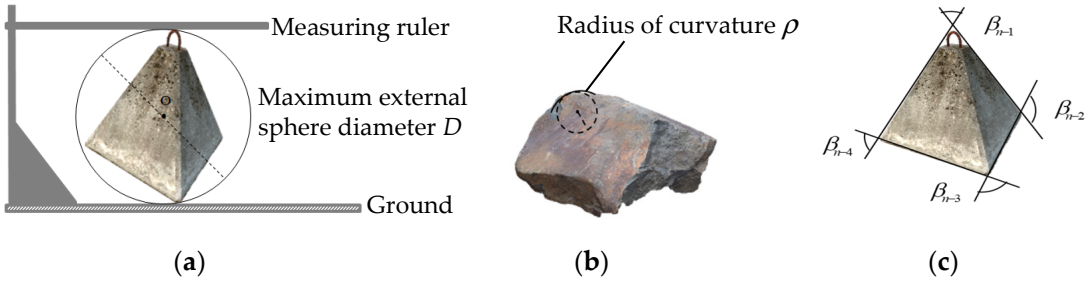

Figure 3. Schematic of stone dimensions: (**a**) maximum external sphere diameter of a stone; (**b**) curvature radius of a stone; (**c**) tip angle of a stone.

3.2.4. Data Analysis

After measurement, the acquired data were statistically analyzed using the maximum external sphere diameter as the independent variable and the radius of curvature and tip angle as the dependent variables, as shown in Figure 4. The collected stones had irregular geometries with sharp edges, flat surfaces, and smooth arcs. The minimum and maximum radii of curvature of the stone surfaces were 3.2 and 29.7 mm, respectively, and the average minimum and maximum radii of curvature were 6.8 and 21.0 mm, respectively. The minimum and maximum tip angles of the stone tips were 42° and 138°, respectively, with an average tip angle of 89°. Although the scatter in these results was high, the radius of curvature of common curved surfaces was 10–20 mm. The typical tip angle was 45–60° for sharp stones and 90–120° for blunt stones within the 100–200 mm outline size range. These values provided a reference for the subsequent definition of common parameters of road debris.

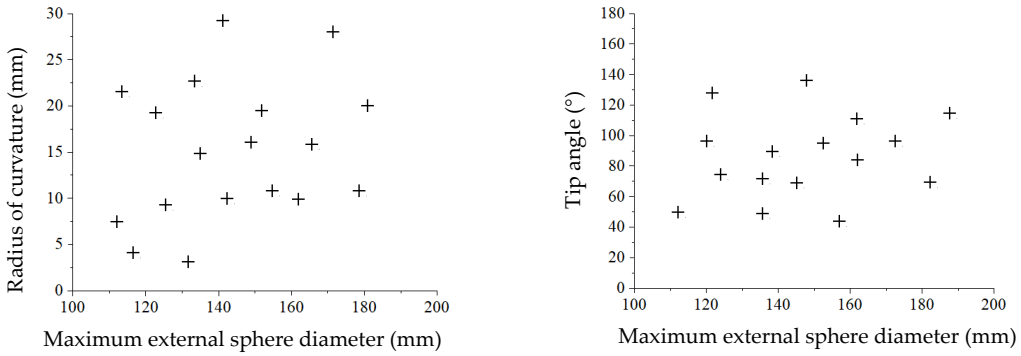

Figure 4. Distribution diagram of stone size parameters.

3.3. Geometric Feature Extraction of Road Foreign Body

In investigations of two fire accidents involving Tesla EV underbody battery packs caused by road debris, metal trailer hooks, and bent metal parts were found. In one of the accidents, a bent metal part pierced the bottom protective plate, which was approximately 6.4 mm thick, leaving a hole approximately 7.6 mm in diameter on the plate. Some metallic materials, such as cemented carbides, have high hardness and strength; thus, they can pierce the battery pack box structure and cause serious damage to the power battery pack under sufficient impact energy. Given the various geometric shapes found in daily life and the engineering of metal products, a simplified geometric feature extraction process was required.

First, using the sample model resource library, 36 samples of metal products with common bending shapes were randomly selected. Then, representative examples were

selected to simplify and extract the key features of the models without changing the overall shape, structure, or consistency of the vehicle bottom collision kinematics. The simplification operations, such as simplification of symmetrical structures, removal of local small features, and conversion of hollow structures to solid structures, are depicted in Figure 5.

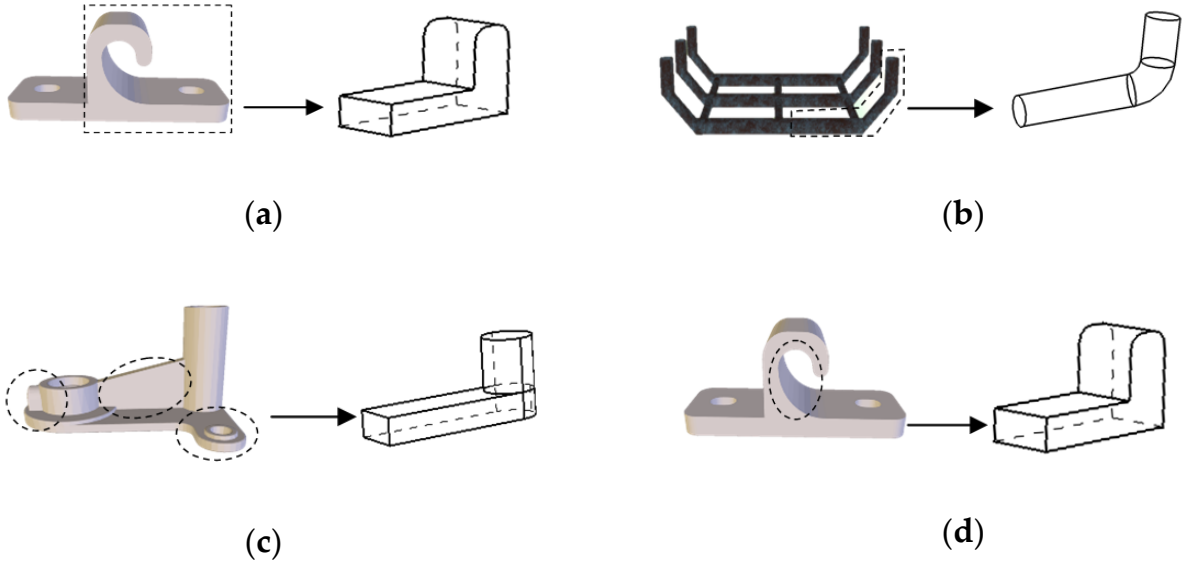

Figure 5. Simplified schematic of metal products: (**a**) Symmetric structure; (**b**) Symmetric structure; (**c**) Remove local small features; (**d**) Solidization of hollow structures.

3.3.1. Simplification of the Symmetrical Structure

As shown in Figure 5a,b, the detailed model contains symmetrical or repetitive structures. To facilitate the parametric construction of the model structure, the symmetrical and repetitive structures were removed, and the kinematic characteristics of the impact of the road foreign body on the vehicle bottom were not altered, thereby simplifying the model.

3.3.2. Removal of Local Small Feature Structures

In the detailed model, local structures such as round holes, ribs, and small bosses appear, as shown in Figure 5c. These small local feature structures were removed without affecting the kinematic characteristics of the impact of the foreign body on the bottom of the vehicle.

3.3.3. Conversion of Hollow Structures to Solid Structures

As shown in Figure 5d, the model has a hollow structure. In the collision with the bottom of the vehicle, the external contour of the foreign body on the road primarily impacts the battery pack box. Its internal structure can be simplified as equivalent to that of a solid structure.

After simplification of the metal objects, the typical working condition of the road foreign body rotating on the bottom of the vehicle was considered, as shown in Figure 6. Although the shape of the road foreign body is complex, as long as its relevant tip features are accurately characterized, the bottom collision kinematics can be determined, which provides a method for establishing the road foreign body model.



Figure 6. Process of rotating hard alloy piercing into the bottom of EV: (**a**) Time A; (**b**) Time B; (**c**) Time C.

In summary, two geometric features of road debris were extracted: tip features and surface contact features. The tip features determine the degree of sharpness or bluntness. During the collision, the contact between the road debris and the vehicle underbody is surface contact. These are the two basic and complementary characteristic parameters of the geometric model of the road foreign body.

3.4. Geometric Parameter Structural Model of Road Debris

Ship grounding is one of the most common and destructive accidents in maritime engineering worldwide. In studies of ship grounding damage, researchers have found that the bottom shape plays an important role in ship grounding events and have proposed a variety of seabed obstacle models (rock, reef, shoal, etc.), with the symmetrical cone model being the most common. Table 2 summarizes the characteristics of the various seabed obstacle models. The polynomial equation and binary function models express changes in seabed rock shapes through the adjustment of parameters. The binary function model achieves the best fitting accuracy and encompasses the simulation capabilities of both the cone and polynomial models. However, it involves many parameters and a complex fitting process.

Table 2. Overview of shape models for underwater obstacles [12].

Shape Model	Parameter	Schematic Diagram	Important Conclusions
Cone model	Tip arc radius, tip angle, height, etc.	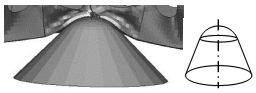	The most commonly used seabed obstacle model in the study
Polynomial Equation model	$z = -y^2/a$ (Common second−order)	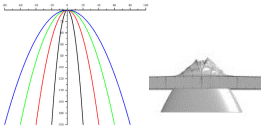	By adjusting the parameters, the change from a sharp small rock to blunt large rock can be realized, and the deformation mode of ship from local tearing to large deformation crushing can be studied.
Binary Function model	Parameters for scaling x and y, variance and mean	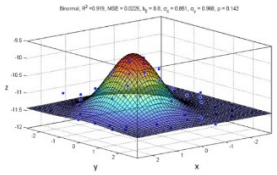	A flexible, best-fitting mathematical model of the shape of the seafloor that can model cones and polynomials

The geometric model of road debris must have variable structural parameters to accurately characterize the main features of road debris, achieve parameterization of the geometric structure, faithfully and objectively reflect collisions with the power battery pack structure, and significantly reduce the time required for model modification and simulation.

Limited studies are available on the impact of road debris on EV underbody power battery packs and on the definition of the characteristics of road debris. The ball-head model was selected by comparing the advantages and disadvantages of various modeling methods for seabed obstacles and by referring to the two-parameter model of foreign road objects proposed by Yong et al. [2]. This model can effectively represent the two major characteristics of road debris, namely, the tip and surface contact characteristics, as shown in Figure 7a. Through flexible adjustment of the parameters, these characteristics can be transformed into the main shapes of road foreign bodies, thereby representing realistic road debris, as shown in Figure 7b.

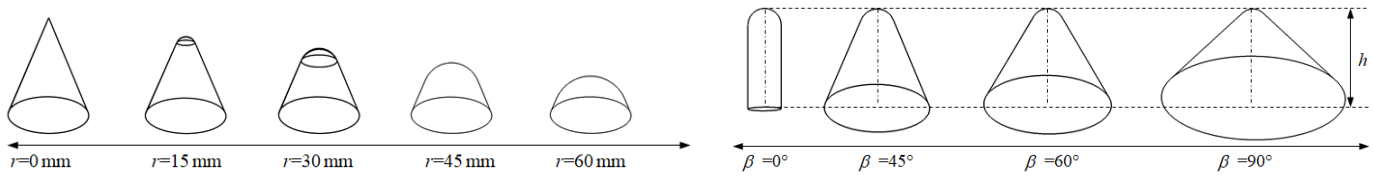

(**a**)

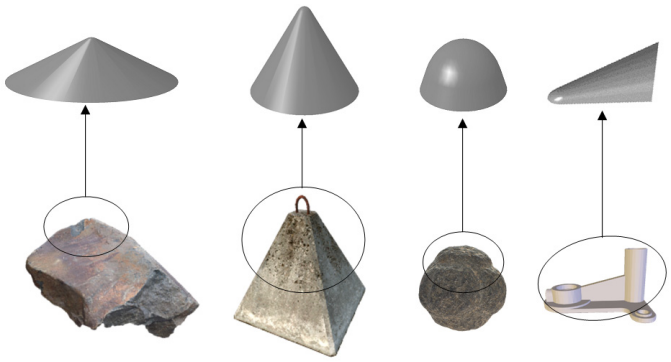

(**b**)

Figure 7. Schematic of road foreign object structure models: (**a**) Geometric parameter structural model of road foreign objects; (**b**) Conversion of road foreign object parameters.

3.5. Impact Modes of Road Debris on the Battery Pack Underbody

Owing to road irregularities, the undulation and pitching motion of the vehicle during travel, and the irregular characteristics of the bottom structure, it is inevitable that the vehicle bottom will encounter road debris. When a vehicle power battery pack strikes such road debris, the object first collides with the lower casing. Owing to the different geometric shapes of foreign bodies on the road and their various motion states before the collision, several impact modes can occur in the interaction between the two, for example, the foreign body on the road rotating on the bottom of the vehicle and horizontal scraping of the vehicle bottom. Different collision forms result in different types of structural damage, which can be divided into three collision effects.

3.5.1. Lever-Type Rotary Puncture

It is assumed that the speed of the vehicle does not change as a result of the impact and that the ground clearance of the vehicle remains constant during vehicle motion. When the bottom of the vehicle hits the object, the two ends of the foreign body on the road form a single-degree-of-freedom mechanism. As shown in Figure 8a, the top of the object contacts the bottom of the vehicle and moves at the same speed as the vehicle at point A.

Simultaneously, the bottom end, point B, of the object remains fixed on the ground, and the object begins to rotate about point B and pierces the bottom plate of the lower box body. Thus, the strong collision impact force causes local damage to the bottom of the vehicle through leverage. The battery pack is subjected to an upward puncture force, and the lower casing, inner frame, passenger compartment floor, and other related structures are subjected to varying degrees of indentation and puncture fracture.



(**a**) (**b**) (**c**)

Figure 8. Modes of foreign objects impacting the bottom of the vehicle on the road: (**a**) Vehicle bottom impact by hard alloy; (**b**) Vehicle bottom crushing concrete; (**c**) Vehicle bottom horizontal scraping impact.

3.5.2. Local Impact Crushing

When the vehicle passes over a speed bump at high speed or strikes round road debris with a large surface area, the bottom structure experiences varying degrees of indentation. When the material strength of the road foreign body is far lower than that of the vehicle bottom, such as in the case of concrete debris, the vehicle passes smoothly after crushing the concrete, as shown in Figure 8b.

3.5.3. Horizontal Scraping Impact

When the road debris is fixed or has a large mass, such as an extended steel bar, it pierces the power battery pack and is dragged for a certain distance until the vehicle stops or the road foreign body separates from the vehicle. The bottom structure of the vehicle is scratched or torn. Depending on the sharpness or bluntness of the road debris, deep and narrow elongated scratches or shallow and wide scratches are produced, respectively, as shown in Figure 8c.

Based on the safety data of road debris collisions, the relationships between the type, geometry, and other attributes of road debris and collision damage were analyzed. Moreover, the main collision characteristic parameters of foreign road objects were extracted, and the following conclusions were drawn:

(1) According to the relevant vehicle damage database, the form of vehicle bottom damage is closely related to the shape and size of road debris. The contact area between sharp road debris and the bottom of the vehicle is small, and the stress is highly concentrated. Thus, the penetration depth into the bottom is the greatest, causing damage to the related structural parts.

(2) Through a simplified analysis of the key features of road debris, two basic features of the main road debris structural shapes were extracted: tip and surface contact characteristics. The triangular pyramid model was selected to establish the geometric parameter structural model of road debris.

(3) The structural model of road debris was combined with the bottom collision kinematic model of the vehicle power battery pack, and the motion characteristics of the power battery pack and road debris were examined for subsequent simulation analysis. Spherical hard metal objects with sharp characteristics were selected for the bottom

impact, and this extreme working condition model was the most harmful to the battery pack.

4. Effects of Underbody Impact on Mechanical Characteristics of the Cell and Pack

4.1. Quasi-Static Compression and Dynamic Impact Tests of Prismatic Cells

4.1.1. Quasi-Static Testing of Cells

The test sample was a prismatic ternary LIB, as shown in Figure 9. The 0.7 mm aluminum shell had a 2.0 mm top cover welded and sealed along the periphery. The internal jellyroll consisted of two independent jellyrolls placed in parallel, with no gap between the jellyroll and the shell. The distance between the jellyroll electrode and the top cover was 7.6 mm. The specific parameters are listed in Table 3.



(**a**) (**b**)

Figure 9. Samples of prismatic lithium-ion cell: (**a**) Prismatic cell; (**b**) Internal jellyroll.

Table 3. Parameters of prismatic ternary lithium-ion battery (LIB).

Parameter	Value
Battery length (X direction)	195 mm
Battery width (Y direction)	51 mm
Battery height (Z direction)	110 mm
Thickness of aluminum housing	0.7~2 mm
Top cover electrode gap (Z-direction)	7.6 mm
Rated voltage	3.7 V
Nominal capacity	160 Ah

The LIB shell could withstand certain tensile and compressive loads under mechanical loading, whereas the internal jellyroll exhibited distinct mechanical properties in different directions owing to the laminated structures of the various materials. To study the mechanical properties of the prismatic LIB, mechanical load tests were performed on the cell, shell, and jellyroll [8,13]. Because the thickness of the shell is only 0.7 mm, a compression test could not be conducted. Considering that the shell is a metallic isotropic material, a quasi-static tensile test was used to obtain its displacement response curves. The tensile samples were cut directly from the aluminum shell, and the tensile test was repeated three times, as shown in Figure 10a. The jellyroll is an anisotropic material. The compression force–displacement response curve of the jellyroll was obtained in the height direction (Z-direction). A D50 mm cylindrical indenter was used to conduct a quasi-static local compression test in the height direction of the jellyroll, as shown in Figure 10b. The stress–strain constitutive curve of the aluminum shell (Figure 10c) and the force–displacement response curve of the jellyroll (Figure 10d) were obtained through three quasi-static tests on the shell and jellyroll.

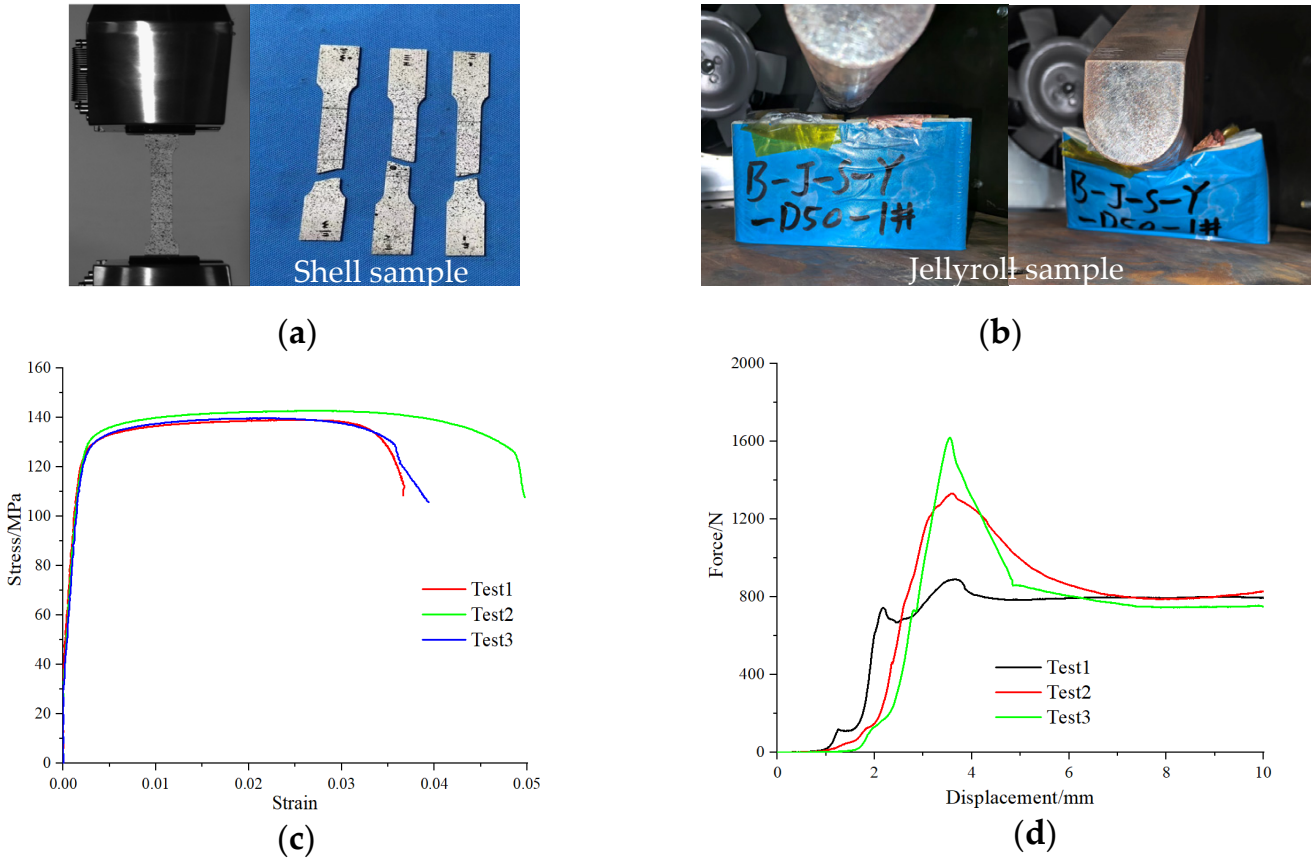

Figure 10. Quasi-static tensile/compression tests and data of the cell sample: (**a**) Shell tensile test; (**b**) Jellyroll compression test; (**c**) Stress–strain constitutive curve of the aluminum shell; (**d**) Force–displacement response curve of the jellyroll.

A local compression test was performed in the Z-direction of the prismatic cell sample (state of charge (SOC) = 0%). The voltage–temperature data acquisition instrument was calibrated to accurately monitor and record the open-circuit voltage and surface temperature. The surface temperature was measured at three locations [14]: the pole, the side of the shell, and the bottom of the shell, as shown in Figure 11a. A spherical indenter with a diameter of 30 mm was used for the quasi-static local compression. To ensure the stability of the initial position of the cell during the entire loading process, a specialized fixture was designed for secure mounting. All tests were conducted at room temperature under sufficient ventilation and were repeated three times, as shown in Figure 11b. After the termination of each loading cycle, unloading was initiated once the monitored voltage and temperature had reached a stable state.

Figure 11c,d show the time–displacement–load–voltage–temperature response curves generated by the two tests. The peak load of sample 1 is 24,322 N at a displacement of 32 mm. The peak load of sample 2 is 25,144 N at a displacement of 27 mm. The deviation in peak load is 3.3%, and the deviation in displacement was 15.6%. The open-circuit voltage (green solid line) and surface temperature (red solid line) of the lithium-ion cell remained constant during the loading process. When the displacement of sample 2 (black solid line) reached approximately 27 mm, a significant decrease in the load (blue solid line) was observed. However, the voltage and temperature remained constant. Therefore, the entire test process did not cause an internal short circuit in the prismatic lithium-ion cell, and no thermal runaway occurred.

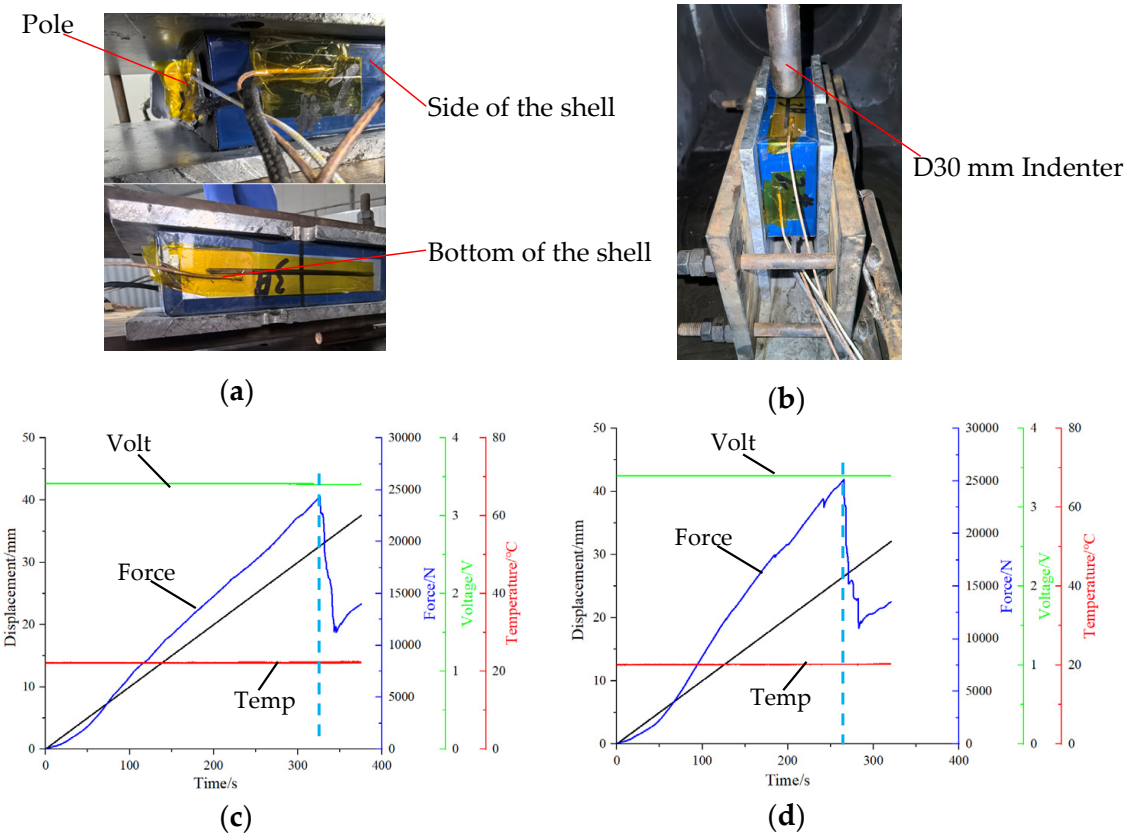

Figure 11. Bottom compression test of prismatic cell: (**a**) Temperature collection at three different locations; (**b**) Cell compression test; (**c**) Time–displacement–load–voltage–temperature response curve of sample 1; (**d**) Time–displacement–load–voltage–temperature response curve of sample 2.

4.1.2. Dynamic Impact Test

The dynamic impact test on the prismatic cell (SOC = 100%) was conducted using the same loading direction, loading position, loading pressure head, fixture, and data acquisition layout as those previously described. The dynamic impact test was performed on a drop-hammer test rig, and the entire test process was recorded using a high-speed camera. Before the test, time synchronization was maintained between the high-speed camera and the data acquisition system. After confirming that all data acquisition systems were operating normally, the impact test was performed, as shown in Figure 12a. The total energy of the dynamic impact test was set to 150 J, with a total counterweight mass of 46 kg and an impact velocity of 2.55 m/s. The data acquisition frequency was set to 20 Hz, and the tests were repeated twice. Figure 12b shows that after the impact test, internal intrusion occurred at the bottom of the prismatic cell, and no shell rupture was observed.

As shown in Figure 12c,d, the surface temperature (solid red line) of the cell did not change during the two impact tests. The peak loads of samples 1 and 2 are 13,317 and 11,689 N, respectively, and the deviation between them is 12.2%. When the displacement of sample 1 (solid black line) reached approximately 20.4 mm, the impact load (solid blue line) decreased significantly. During this process, the open-circuit voltage (green solid line) of the cell fluctuated significantly and then returned to a stable state. The voltage and temperature of the cell did not change after the test samples were allowed to stand for an extended period. The bottom impact did not directly lead to a serious internal short circuit in the cell, but it caused an obvious fluctuation in the open-circuit voltage owing to the buckling of the electrode stack inside the cell. This resulted in a micro-short circuit in the LIB [15,16]. Significant safety hazards may appear in subsequent charge–discharge cycles.

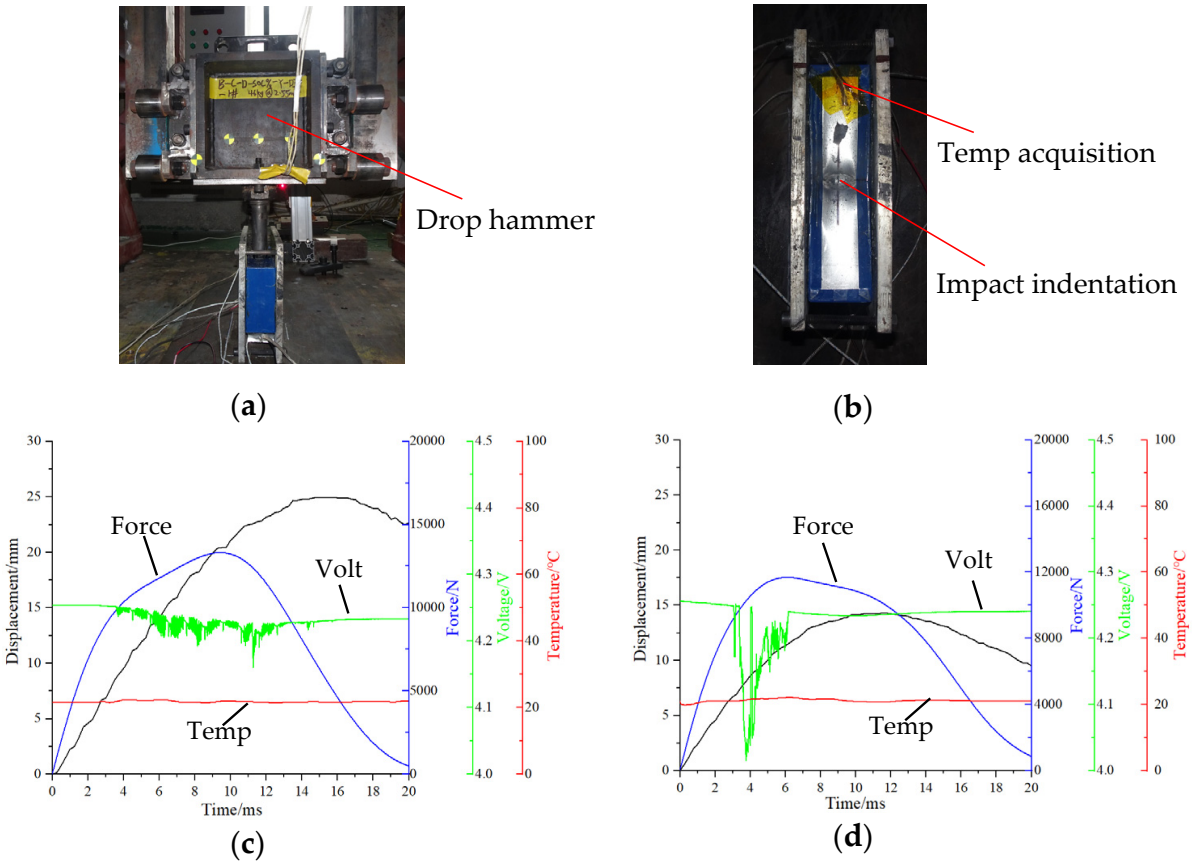

Figure 12. Dynamic impact test: (**a**) Prismatic cell impact test; (**b**) Prismatic cell impact indentation; (**c**) Impact response curve of sample 1; (**d**) Impact response curve of sample 2.

4.2. Battery Pack Bottom-Ball Impact Test

According to the research and analysis, the damage to the bottom of the battery pack caused by road debris results from bottom scraping and impact; in particular, local impact can cause the most serious damage to the bottom of the battery pack. Therefore, the battery pack was first pretreated for the bottom impact condition test. The battery pack was discharged twice consecutively to a residual capacity of less than 3% of the rated capacity. The battery pack was then charged to the cutoff voltage at a rate of 1/3C and allowed to stand for 30 min until 80% of full charge was reached. Finally, the insulation resistance of the battery pack and the impact positions at the bottom of the battery pack were measured. Photographs and data were obtained throughout the entire process, as shown in Figure 13a. The battery pack was fixed to the impact test bench using a specialized fixture to establish the three impact positions, as shown in Figure 13b. Before the impact test, the open-circuit voltage and surface temperature of the battery cells inside the battery pack were measured and confirmed to be normal at the impact positions. The data sampling frequency throughout the test was 200 Hz, and data acquisition continued for an additional 20 min after completion of the test. The diameter of the bottom impact ball was 30 mm, with a total impact energy of 150 J, as shown in Figure 13c.

After the impact test was completed, the battery pack was carefully disassembled while still energized. The deformation of each component was accurately obtained after the test. The bottom guard plate, water-cooling plate, and battery cell were evaluated based on the disassembly sequence. As shown in Figure 14, at impact position 1, the impact deformation depth of the bottom guard plate was approximately 5.72 mm. The liquid cooling plate deformed at the edge of the flow channel to a depth of 5.26 mm, whereas the cell showed a deformation of 2.85 mm at the center of its bottom surface. At impact

position 2, the impact deformation depth of the bottom guard plate was approximately 7.38 mm, the liquid cooling plate deformed in the middle of the flow channel with a depth of 5.54 mm, and the cell showed a deformation of 3.11 mm at its bottom edge. At impact position 3, the impact deformation depth of the bottom guard plate was approximately 6.63 mm, the liquid cooling plate deformed at the non-flow channel position with a depth of 3.58 mm, and the deformation depth between two adjacent cells was 2.61 mm.

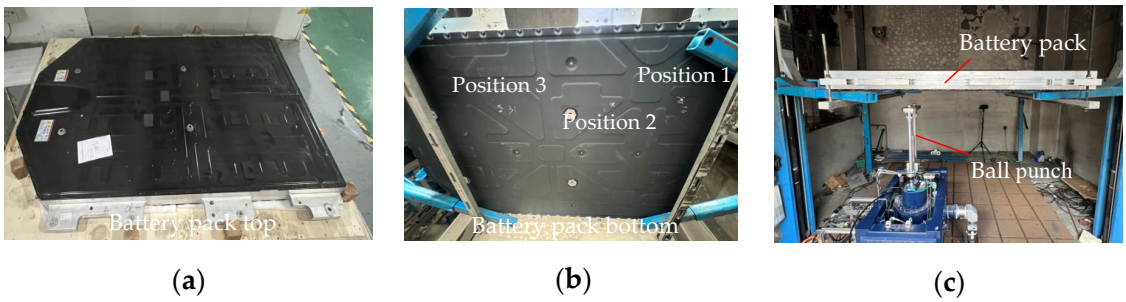

Figure 13. Battery pack bottom-impact test: (**a**) Battery pack (state of charge (SOC) = 80%); (**b**) Battery pack bottom impact position; (**c**) Battery pack bottom-ball impact test.

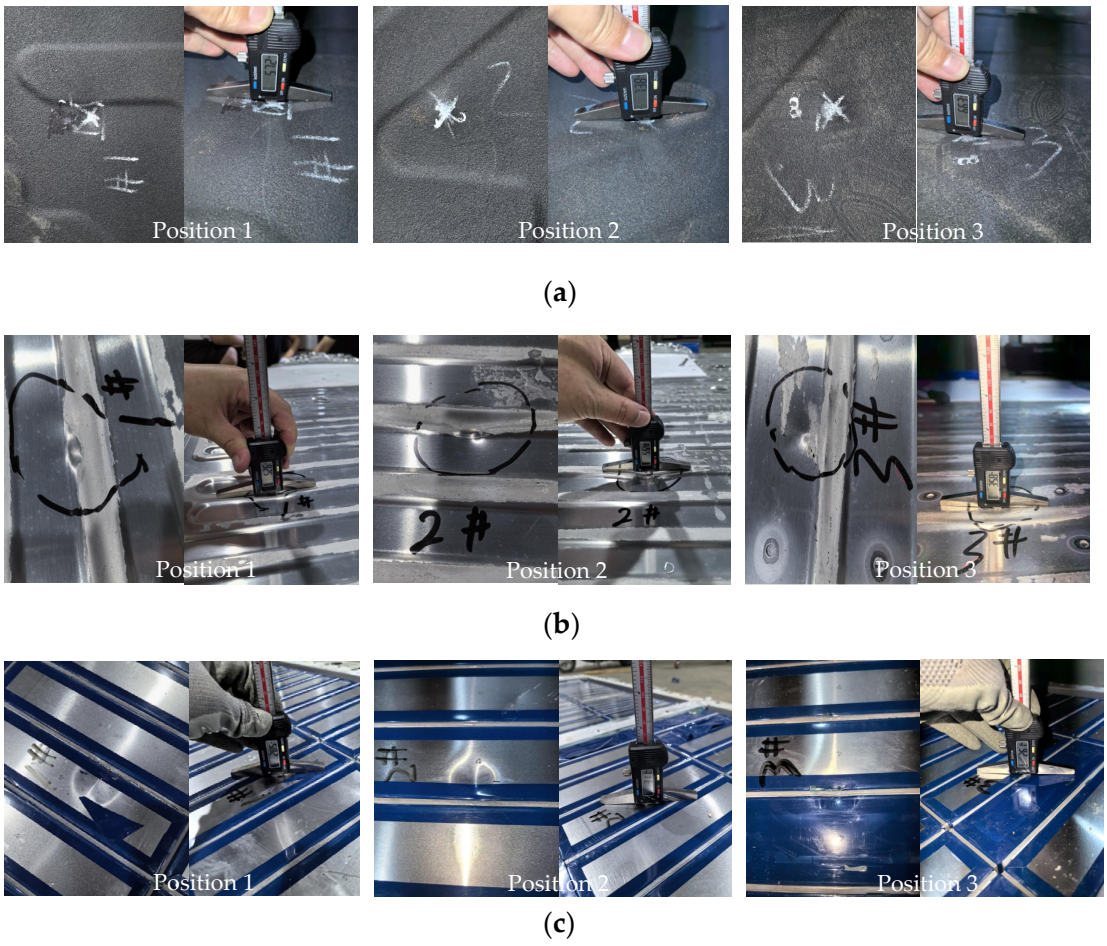

Figure 14. Deformation of the battery pack components after impact testing: (**a**) Deformation of the bottom guard plate; (**b**) Deformation of the liquid cooling plate; (**c**) Deformation of the cell.

According to the evaluation of each component, local deformation occurred in each layer, with the magnitude of deformation progressively decreasing through each subsequent layer. As listed in Table 4, among the three impact positions, the component at position 2 exhibited the largest deformation. This position was in the middle of the flow

channel of the liquid cooling plate, and the flow channel interface underwent serious deformation, which may have led to a decrease in the performance of the liquid cooling plate. The ratio of deformation of the cell to deformation of the bottom guard plate at position 1 was the largest. Considering that the impact tests at the three positions did not cause an internal short circuit in the cell, the test results at impact position 1 were selected for the benchmarking and verification of the subsequent simulation to ensure consistency with the dynamic impact test position of the cell.

Table 4. Localized deformation of different components of the power battery pack.

Position	Deformation (mm)			Ratio (%)
	Bottom Guard Plate	Cold Liquid Plate	Cell	
1	5.72	5.26	2.85	49.8
2	7.38	5.54	3.11	42.1
3	6.63	3.58	2.61	39.4

5. Simulation Analysis of LIB and Battery Pack Underbody Impact

5.1. LIB Homogenization Model

The internal jellyroll is a fundamental component of cells and battery packs. Consequently, an accurate FEM for the jellyroll was developed and calibrated. The FEM was developed in the LS-DYNA environment to satisfy the simulation requirements of the compression and impact conditions. The alternating layered structure of the jellyroll was neglected and simplified to a homogeneous structure to mitigate convergence and computational efficiency issues during simulation calibration.

A finite element homogenization mechanical model was developed according to the geometric dimensions of the internal jellyroll listed in Table 3. As shown in Figure 15a, a hexahedral mesh with an element size of 4 mm was selected for mesh generation of the model. Six layers of elements were placed along the Y-direction of the system coordinate axis, for a total of 7075 solid elements. To simulate the double-laminated structure of the jellyroll shown in Figure 9b, two identical jellyroll models were stacked in the Y-direction of the coordinate axis. Elements at the shared contact surface were not assigned shared nodes; instead, contact (CONTACT_AUTOMATIC_SINGLE_SURFACE) was used in the simulation. The volume fraction of the coating material in the jellyroll of the LIB was the highest, demonstrating strain-hardening characteristics under compressive loading. However, the in-plane tensile strength was low. Therefore, the material model for the jellyroll was characterized by selecting MAT_063 (MAT_CRUSHABLE_FOAM). The compression constitutive equation of the jellyroll was inversely calibrated using the quasi-static compression test curve shown in Figure 10d.

It was assumed that the compression constitutive curve of the jellyroll under a D50 mm cylindrical indenter (Suzhou Automobile Research Institute, Tsinghua University, China) satisfied the following power function form [17]

$$\sigma = \sigma_0 + K\varepsilon^n \quad (1)$$

where σ_0 denotes the initial stress, K is the material parameter, and n is the hardening exponent. The fitting method for Equation (1) is referred to in Appendix A.1.

The material model MAT_020 (MAT_RIGID) was selected to represent both the indenter and the bottom supports. The mesh for these components employed quadrilateral shell elements with a size of 5 mm, as shown in Figure 15b. The interaction between the rigid bodies and jellyroll was simulated using contact (CONTACT_AUTOMATIC_SURFACE_TO_SURFACE). Contact control SOFT = 2 was used to

prevent cell distortion caused by the significant difference in contact stiffness between the rigid indenter and the jellyroll. During the simulation of the quasi-static compression process, rigid displacement loading (BOUNDARY_PRESCRIBED_MOTION_RIGID) was used to define the compression motion trajectory of the indenter along the negative Z-direction. The bottom support was fully constrained in all six degrees of freedom. For all elements, ELFORM = 2 was selected. The coefficient of friction was set to 0.3 [17] for all contact surfaces. Hourglass control was used during the simulation, with IHQ = 5 and the default control factor HQ = 0.1. The parameters of Equation (1) were fitted by inverse calibration: σ_0 = 0.1, K = 30 MPa, and n = 1.1. The fitted constitutive equation was input into the material model of the jellyroll, and a quasi-static compression simulation was carried out using a D50 mm cylindrical indenter. The results are shown in Figure 15c. The peak load of the simulated force–displacement curve (blue dashed line) was slightly higher than that of test 1 (black solid line), but the overall trend remained consistent.

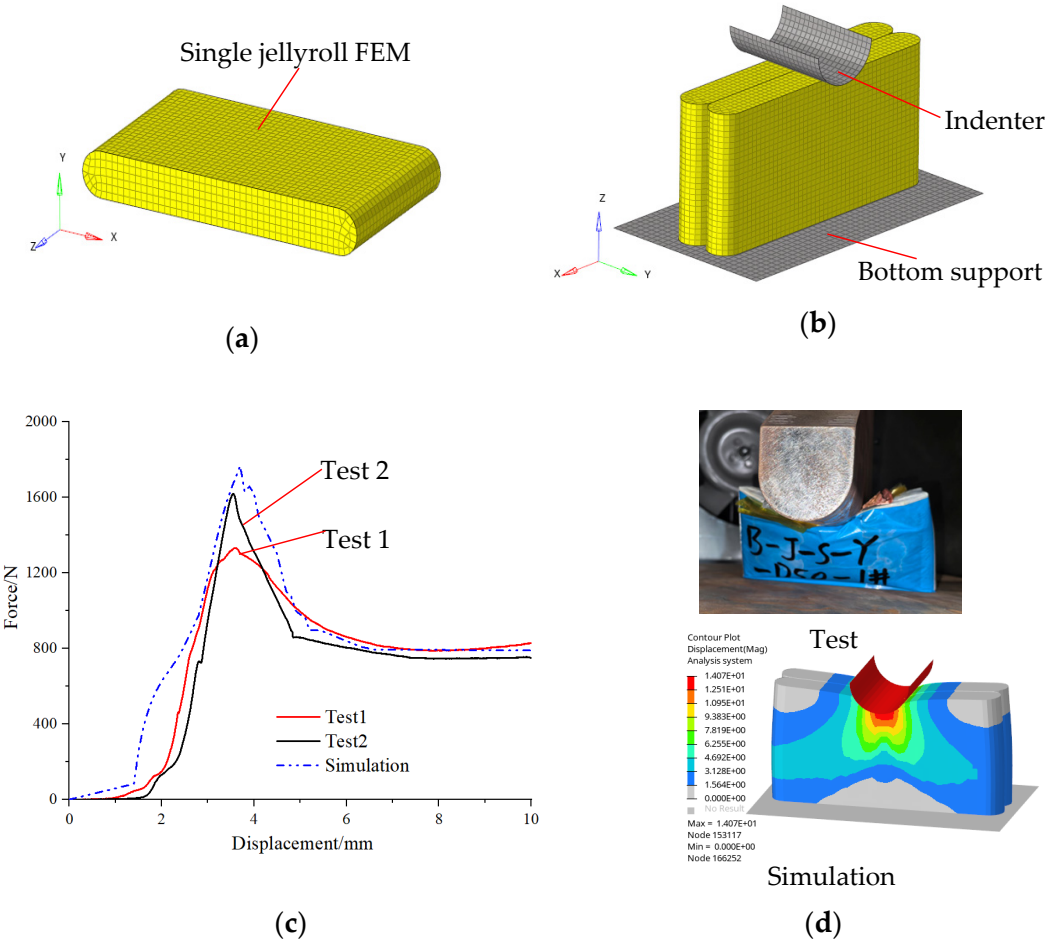

Figure 15. Internal jellyroll compression finite element model (FEM) and simulation analysis: (**a**) Single jellyroll FEM; (**b**) Two identical jellyroll compression FEMs along the Z-direction; (**c**) Comparison of quasi-static compression test and simulation curves for the jellyroll; (**d**) Comparison of the test image and simulation displacement contour plot.

The prismatic cell comprised a jellyroll, electrolyte, shell, end cap, and pole. The shell, end cap, and pole were modeled using the previously calibrated jellyroll model, and the electrolyte was neglected. The meshes of the shell and end-cap models employed quadrilateral shell elements with a size of 4 mm, and the mesh of the pole model employed hexahedral solid elements with a size of 4 mm. The entire prismatic cell model contained 18,964 elements, as shown in Figure 16a. MAT_024 (MAT_PIECEWISE_LINEAR_PLASTICITY) was

selected as the material model for the shell, end cap, and pole. The constitutive curve was the uniaxial tensile test curve of the shell (Figure 10a). Contact (CONTACT_AUTOMATIC _SINGLE_SURFACE) was used to simulate the interaction between the jellyroll and the shell. A binding connection (CONTACT_TIED_SURFACE_TO_SURFACE) was used to simulate the poles and end caps. Figure 16b shows the FEM of a D30 mm spherical indenter compressing a homogenized LIB. The meshes of the spherical indenter and the specialized fixture employed quadrilateral shell elements with a size of 5 mm. The material model was characterized using MAT_020. The contact stiffness setting was consistent with that used in the jellyroll simulation.

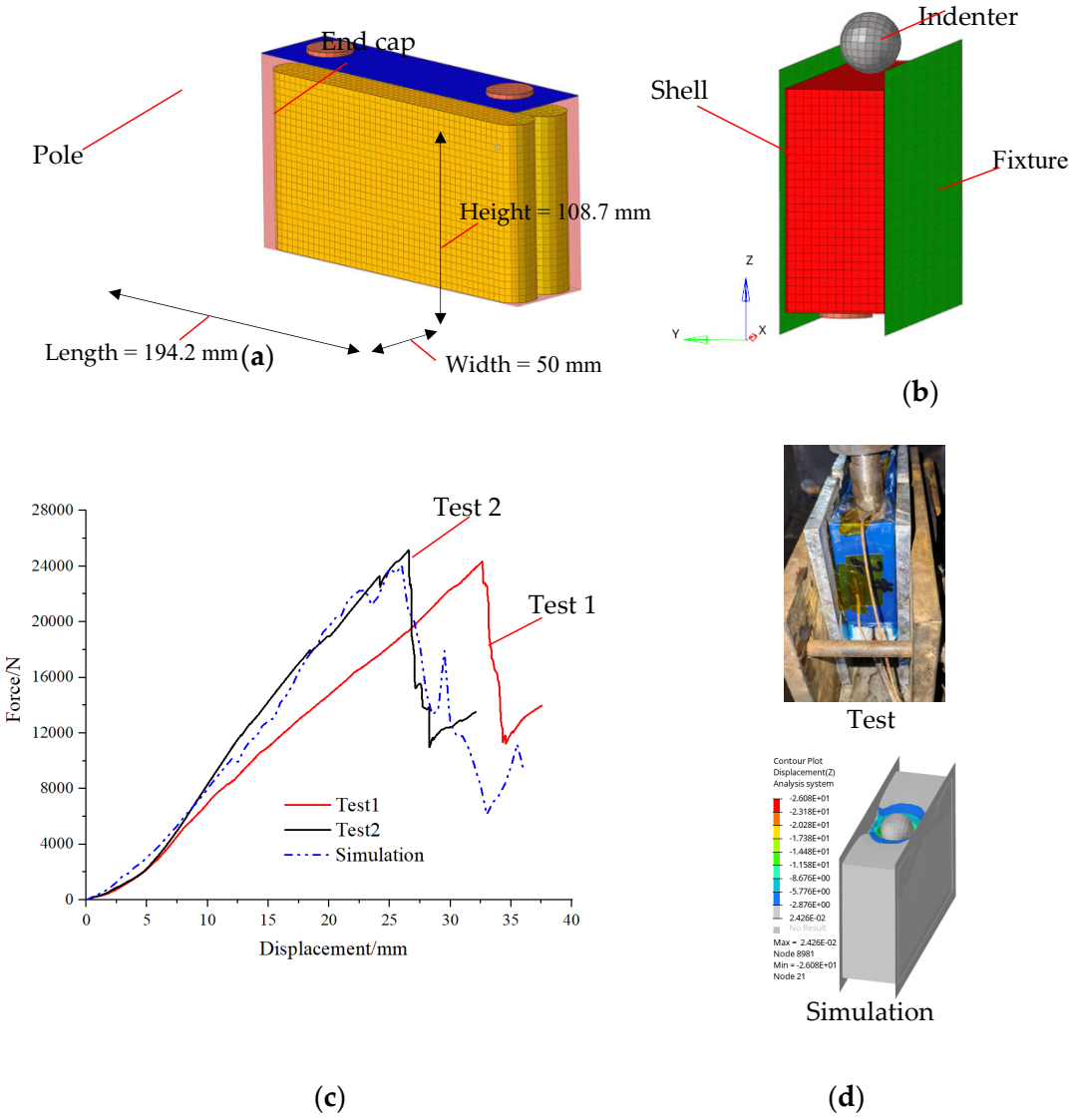

Figure 16. Prismatic cell compression FEM and simulation analysis: (**a**) Cell FEM; (**b**) Cell compression FEM along the Z−direction; (**c**) Comparison of quasi−static compression test and simulation curves for the prismatic cell; (**d**) Comparison of the test image and simulation displacement contour plot.

The actual buckling behavior could not be accurately characterized in the simulation of the homogenized jellyroll model. Therefore, the physical phenomenon of jellyroll compression failure was neglected, focusing instead on the macroscopic force–displacement response curve and peak load. The element deletion method (MAT_ADD_EROSION) was used to calibrate model failure using the maximum equivalent stress. The maximum equivalent stress was set to σ_{max} = 26 MPa. A comparison of the simulation and experimental

results is shown in Figure 16c. The comparison reveals a difference in the position of the peak load between the two compression tests, and the simulation curve (blue dotted line) was consistent with the test 2 curve (black solid line). Under the load of the D30 mm spherical indenter, test 2 reached a peak load of 25,144 N and a failure displacement of 27 mm, whereas the simulation yielded a peak load of 24,057 N and a failure displacement of 26.0 mm. The deviations in peak load and failure displacement were 4.3% and 3.8%, respectively. The homogenized model of the prismatic LIB calibrated using the maximum equivalent stress failure criterion satisfactorily predicted the force–displacement response curve of the quasi-static test.

LIBs exhibit a strain rate effect during dynamic impacts. This is primarily attributable to two reasons. The first is the strain rate effect of the jellyroll component materials. Experiments [18] performed involved compression tests on the jellyroll for a wide range of strain rates. Specifically, jellyrolls in the prismatic LIB cells were subjected to compressions at various strain rates. The test results showed that the initial peak stress decreased for strain rates in the range of 9×10^{-4} to 657/s. The second is the dynamic effect of the electrolyte during impact loading. In this context, experiments [19] showed that dry cells without electrolyte exhibited a relatively weak strain-rate dependence, which could be predicted from a small number of quasi-static tests in a straightforward manner. By contrast, wet cells containing electrolyte showed significant strain-rate dependencies in terms of material stiffness as well as failure force, in turn revealing a strong dependence on the cell form factor. According to previous experimental studies, the strain-rate effect of the jellyroll material is not obvious. The main source of the strain rate effect of the jellyroll is considered to be the additional viscous force caused by the rapid flow of the electrolyte in the jellyroll under dynamic loading. This indicates that, in the dynamic impact area, the greater the electrolyte content, the stronger the dynamic effect. Therefore, the strain rate effects of LIBs differ considerably in dynamic impact tests along different directions. When dynamic impact is exerted along the Y-direction (large surface), the LIB is likely to show a strong strain-rate effect owing to the high electrolyte content over the entire large surface area. The dynamic impact along the X-direction (side) and Z-direction (bottom) exhibited a weak strain-rate effect. In summary, the impact simulation ignored the influence of the electrolyte strain-rate effect.

The material parameters, constraint conditions, and contact stiffness settings in the dynamic impact simulation were consistent with those in the quasi-static simulation. The failure calibration method also involved deleting the failure element (MAT_ADD_EROSION) with a maximum equivalent stress σ_{max} = 30 MPa. The simulation and experimental results are presented in Figure 17. The peak load and local intrusion were identified as the main differences between the two impact tests. In test 1 (red solid line), the local intrusion was 9.13 mm (Figure 17a), and the peak load was 13,317 N (Figure 17c). In test 2 (solid green line), the local intrusion was 10.68 mm (Figure 17b), and the peak load was 11,689 N (Figure 17c). The variability between tests was mainly attributable to differences in manufacturing consistency among the lithium battery cells. The time–displacement response curve (blue dotted line) generated by the simulation was in good agreement with that of test 1. The local intrusion of the simulation model was 14.9 mm (Figure 17d), and the peak load was 12,778 N (Figure 17c). Because the strain-rate effect was ignored in the simulation, the local intrusion was greater than the experimental intrusion. Considering that the two impact tests did not cause an internal short circuit in the LIB, the local intrusion of 10.68 mm observed in test 2 was selected as the intrusion threshold for an individual LIB cell without internal short circuiting under the impact of the ball at the bottom of the power battery pack.

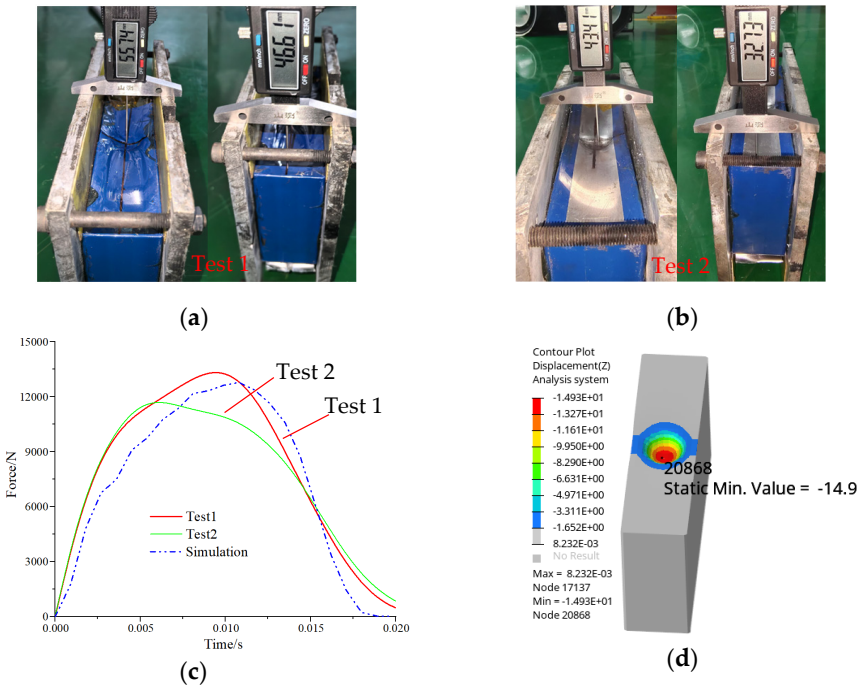

Figure 17. Prismatic cell dynamic impact test and simulation analysis: (**a**) Cell intrusion displacement in test 1; (**b**) Cell intrusion displacement in test 2; (**c**) Comparison of dynamic impact test and simulation curves for the cell; (**d**) Cell simulation displacement contour plot.

5.2. Development of Battery Pack Bottom-Impact FEM

To develop an FEM of a power battery pack, simplification of the parameters is essential. The battery management system (BMS) and high/low-voltage harness model are cumbersome and complex, and have a negligible impact on the simulation results. The battery cells are connected in series and parallel to form a module. In this study, to ensure computational efficiency in the simulation, the modules were divided into equivalent and real modules. The equivalent module was modeled directly using a homogenized module. The battery pack box body was formed as a welded cavity body. The upper cover plate, cooling liquid plate, and bottom guard plate were connected using bolts. The battery modules were bonded using structural glue. In the modeling process, the welds between the cavities were refined. In the real module, the actual configuration of the battery cells and connecting parts was refined. The damping foam and glue (thermally conductive structural glue and sealant) inside the entire battery pack were modeled according to their actual thicknesses. The cavity, cavity welds, lifting lug bushings, homogenized module, PC board, and glue of the battery pack were simulated using solid elements. The upper cover plate, cooling liquid plate, and bottom guard plate were simulated using shell elements. Modified polypropylene (MPP) foam—possessing lightweight, impact resistance, vibration resistance, and thermal insulation properties—was incorporated between the bottom guard plate and the cooling liquid plate. The FEM was characterized using the MAT_001 material model and hexahedral elements. The lower surface of the bottom guard plate was provided with a polyvinyl chloride (PVC) coating layer, which provides impact resistance and corrosion resistance. The FEM was also characterized using the MAT_024 material model and 1 mm thick shell elements. The mechanical property parameters of the MPP foam and PVC coating materials are presented in Appendix A.2. The contact mode between the components of the battery pack was simulated using a binding connection (CONTACT_TIED_SURFACE_TO_SURFACE). All bolt connections were simulated using rigid elements. The element sizes of the cavity, cavity welds, upper cover plate, cooling liquid plate, bottom guard plate, lifting lug bushings, PC board, and other parts were set

to 4 mm, whereas those of the homogenized module, foam, and glue were set to 10 mm. The entire battery pack model contained 5,735,161 elements. Finally, a refined FEM of the battery pack was established, as shown in Figure 18.

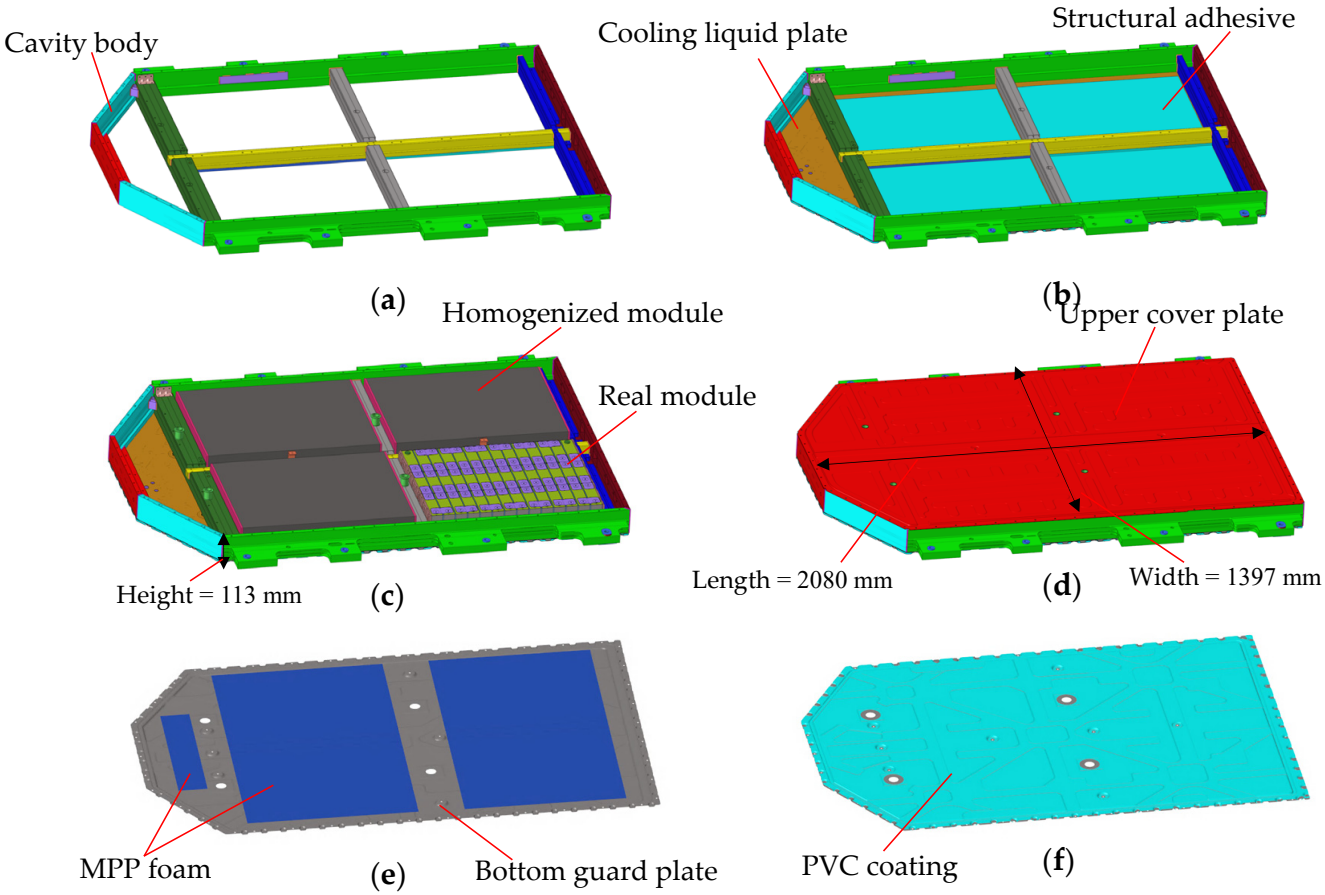

Figure 18. Battery pack FEM: (**a**) Cavity body model; (**b**) Cooling liquid plate and structural adhesive model; (**c**) Homogenized module and real module model; (**d**) Upper cover plate model; (**e**) Modified polypropylene (MPP) foam and bottom guard plate model; (**f**) Polyvinyl chloride (PVC) coating model.

According to the bottom-ball impact test, the impact speed at position 1 was 5.5 m/s, with a total impact energy of 150 J. The ball-punch model was characterized using the MAT_020 material model and hexahedral elements. The weight of the ball-punch model was set to 10.1 kg based on the total impact energy. The six degrees of freedom of the eight bushing mounting points on both sides of the battery pack cavity beam were constrained. CONTACT_AUTOMATIC_SURFACE_TO_SURFACE was used to simulate the contact between the bottom guard plate and the ball punch, with a friction coefficient of 0.3, as shown in Figure 19a. The total duration of the impact was set to 0.012 s, with a data output time interval of 2×10^{-4} s and a calculation time step of 1×10^{-7} s. A 64-core cloud server platform was used for computation, with a total calculation time of approximately 13 h. The energy changes during the simulation process were analyzed to ensure the reliability of the calculation accuracy, as shown in Figure 19b. Throughout the impact process, the total energy of the system remained stable at 151.730 J, and the hourglass energy was 1.434 J, accounting for 0.95% of the total energy. The hourglass energy was less than 5%, thus satisfying the requirements for calculation accuracy and reliability.

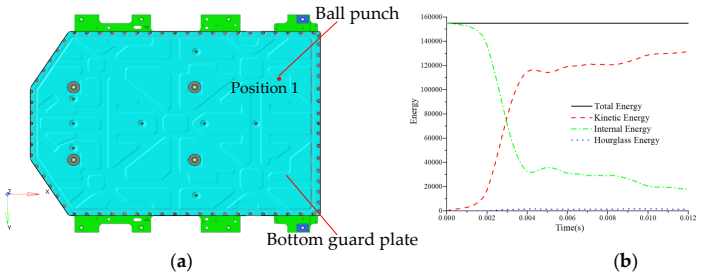

Figure 19. Battery pack bottom impact FEM: (**a**) Bottom impact model; (**b**) Energy change diagram in impact simulation.

To verify the accuracy of the simulation results for the bottom-ball impact on the battery pack, the simulation results of several key components of the battery pack were analyzed and compared. According to the results of impact test position 1 (Table 4), the impact deformation depths for the bottom guard plate, cooling liquid plate, and cell were approximately 5.72, 5.26, and 2.85 mm, respectively. Considering that the test results were measured using a depth gauge with a contact outer diameter of 85 mm (Figure 20a), reference points were extracted in the simulation to ensure a horizontal distance of 42.5 mm. Hence, more accurate simulation results were obtained for each component. Figure 20b shows that the straight-line distance from the lowest point of the simulated deformation of the bottom guard plate to the extraction reference point, the vertical depth from the bottom, and the horizontal distance were 43.1, 6.8, and 42.6 mm, respectively, satisfying the test measurement standards. Using the same method for extraction, the vertical depths of the simulated deformation of the cooling liquid plate and the cell were 6.1 mm (Figure 20b) and 4.3 mm (Figure 20b), respectively.

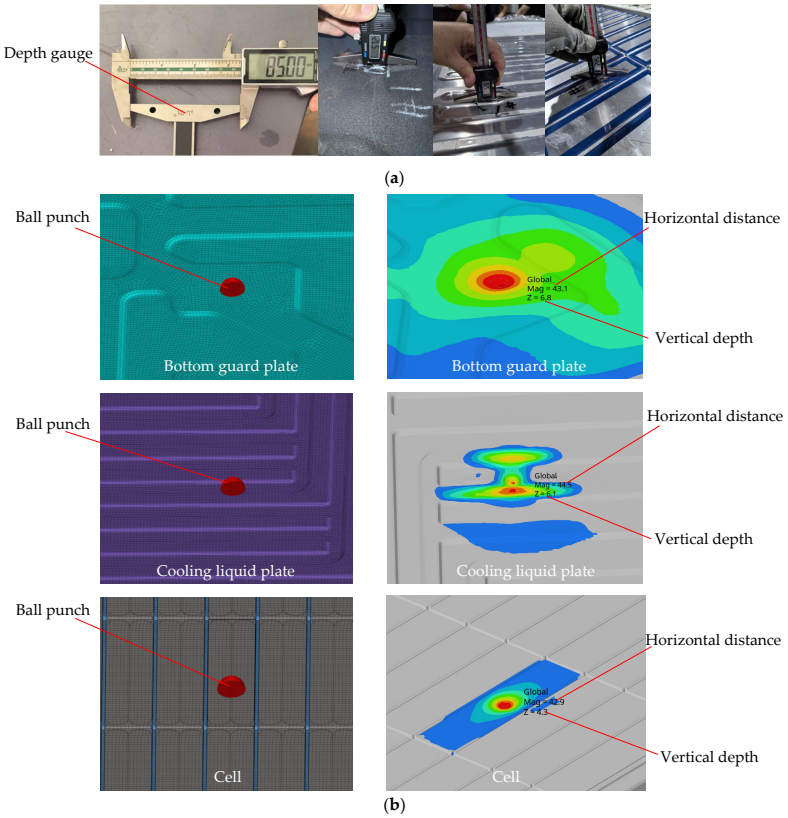

Figure 20. Simulation results of the battery pack bottom impact: (**a**) Depth gauge with a contact outer diameter of 85 mm; (**b**) Simulated impact deformation depths of the bottom guard plate, cooling liquid plate, and cell.

According to these research results, the maximum deformation at the bottom of the cell caused by the bottom ball impact on the battery pack was 2.85 mm, which was lower than the deformation of the cell under dynamic impact, 10.68 mm (Figure 17b). This satisfies the safety requirements for preventing short circuits and fires in the LIB. As presented in Table 5, the deviations between the simulation and test results for the bottom guard plate and cooling liquid plate were 18.8% and 15.9%, respectively, both of which were less than 20%. By contrast, the deviation between the simulation and test results for the cell was 50.8%.

Table 5. Comparison of test and simulation results for different components of the battery pack.

Component	Deformation (mm)		Ratio (%)
	Test 1	Simulation 1	
Bottom guard plate	5.72	6.8	18.8
Cold liquid plate	5.26	6.1	15.9
Cell	2.85	4.3	50.8

6. Conclusions

First, the geometric parameters of road debris and the form of the bottom impact on the power battery pack were defined and characterized, providing a reference for the failure modes resulting from the impact of road debris on the vehicle battery pack underbody. Quasi-static compression and dynamic impact tests were performed on a prismatic LIB to investigate the macroscopic mechanical properties and deformation failure mode of the battery cells. A bottom-ball impact test was performed on a power battery pack, and the deformation responses of its critical components were evaluated. This test revealed that the deformation of the battery cells caused by the pack-level bottom impact was lower than that observed in the dynamic impact tests of the individual cells. This confirmed that the battery pack did not undergo thermal runaway. Finally, based on the experimental data, a homogenized FEM for LIB cells and a comprehensive FEM suitable for assessing the impact, collision, and compression safety of power battery packs were successfully developed.

Through a simplified analysis of the key features of road debris, two fundamental structural features were extracted: tip and contact surface features. A hard spherical metal object was selected for the bottom impact study because this specific condition can genuinely and objectively reflect the accident safety of the power battery pack. Neither the quasi-static compression test nor the dynamic impact test performed on individual cells resulted in an internal short circuit or thermal runaway. The constitutive equation and failure parameters of the cell were determined by fitting a quasi-static compression test curve, allowing a homogenized FEM of the cell to be established. This model can accurately predict the macroscopic force–displacement response curve for a quasi-static compression test. The time–displacement response curves generated by the dynamic impact simulation with the homogenized model were in good agreement with the experimental results. However, the magnitude of the simulated local intrusion was greater than that observed experimentally. This discrepancy arises because the model neglects the dynamic strain rate effect of the electrolyte. Therefore, the local intrusion of 10.68 mm observed in the dynamic impact test was selected as the threshold for the LIB to avoid triggering an internal short circuit. A bottom-ball impact test (using a 30 mm diameter ball punch) was performed on a power battery pack with a total energy of 150 J. Following this test, the battery pack underwent careful disassembly while still energized, and the deformation responses of the bottom guard plate, cooling liquid plate, and cells were evaluated. By comparing the simulation and experimental results, the deformation deviations of the bottom guard plate

and cooling liquid plate were found to be 18.8% and 15.9%, respectively, both below the 20% threshold. However, the deviation in the cell deformation was significantly higher (50.8%).

This phenomenon may have resulted from four factors: (1) the influence of the dynamic strain rate of the electrolyte within the cell was ignored; (2) a considerable quantity of cooling liquid was present inside the flow channels of the battery pack cooling liquid plate, and during the modeling process, the cooling liquid was ignored, leading to a decrease in the accuracy of the battery pack FEM; (3) the jellyroll was affected by the strain rate; and (4) the effect of jellyroll homogenization within the cell.

Further research is required to improve the accuracy of the cell FEM. For example, the pore fluid movement feature developed based on geological materials can provide a modeling approach for the fluid–solid interaction inside cells and enable the development of a homogenized cell FEM with fluid–solid coupling [19]. It is also possible to consider introducing a simple viscous term in the homogenized jellyroll to approximate the strain-rate effect of the electrolyte, but this method has not yet been verified. Another method is to model the jellyroll according to the actual discrete layered structure, including the electrode coating, metal collector, and separator [20]. For the coating material, only the mechanical properties pertaining to compression hardening need to be considered, whereas for the separator material, the more significant anisotropy characteristics and dynamic strain rate effects should be factored in [21]. The refined cell FEM demonstrates capabilities for accurately predicting battery behavior under impact loading and the internal failure process of the battery. However, it would also require additional computing time and thereby reduce efficiency for engineering applications.

Although some deviations in accuracy were noted between the test and simulation results for cell deformation in the FEM for bottom impact, the FEM nonetheless reveals the deformation conditions of all key components. This conclusion provides certain suggestions for improving the safety of the bottom-impact performance of the battery pack. In the future, the accuracy of the battery pack FEM can be optimized by continuously improving the dynamic performance parameters of the cells and component materials to meet the simulation accuracy requirements.

Author Contributions: Conceptualization, L.L. and F.L.; Methodology, Z.L.; Software, Z.L.; Validation, Z.L.; Formal analysis, Z.L.; Investigation, J.C.; Resources, Y.W.; Writing—original draft, Z.L.; Writing—review & editing, L.L., J.C. and F.L.; Supervision, Y.W. All authors have read and agreed to the published version of the manuscript.

Funding: This research received no external funding.

Data Availability Statement: The original contributions presented in this study are included in the article. Further inquiries can be directed to the corresponding author.

Acknowledgments: This work was supported by The Second Generation Magazine Battery Safety Project (XBW).

Conflicts of Interest: The authors, Zhijie Li and Yuchao Wang, were employed by Research and Development Center, Guangzhou Automobile Group (China). The remaining authors declare that the research was conducted in the absence of any commercial or financial relationships that could be construed as a potential conflict of interest.

Abbreviations

EV	Electric vehicle
LIB	Lithium-ion battery
FEM	Finite element model
ρ	Radius of curvature

β	Tip angle
σ_0	Initial stress
K	Material parameter
n	Hardening exponent

Appendix A

Appendix A.1. The Equation Parameter Fitting Method

The reverse calibration method is adopted for Equation (1):

$$\sigma = \sigma_0 + K\varepsilon^n$$

Considering previous empirical values, we fixed the range of K at 20–65, and that of n as 1.1–1.4. The larger the K value, the greater the overall slope of the curve; likewise, the larger the n value, the more evident the overall curvature of the curve. According to the test results shown in Figure 10d, for a constant n, different K values were considered in the simulation. After calibration of the K value, different n values were then considered in the simulation until the simulation results approached the test results with the best trend, as shown in Figure A1.

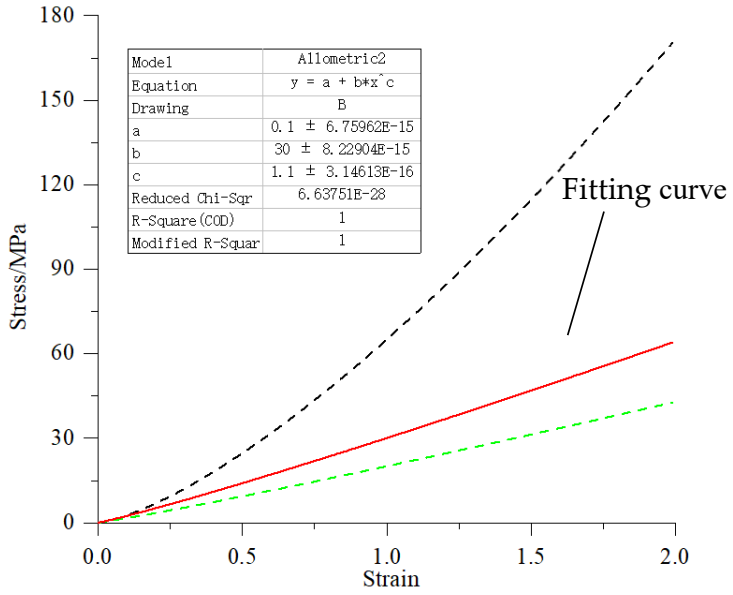

Figure A1. Fitting curve of the jellyroll constitutive equation.

Appendix A.2. The Mechanical Properties of the Material Model

Material type 1 (MAT_001): This is an isotropic elastic material and is available for beam, shell, and solid elements (see Table A1).

Rigid material type 20 (MAT_020) provides a convenient way of turning one or more parts composed of beam, shell, or solid elements into a rigid body. Approximating a deformable body as rigid is a preferred modeling technique in many real-world applications. Elements that are rigid are bypassed during element processing, and no storage is allocated for history variables; consequently, the rigid material type is very cost-efficient.

Piecewise-linear-plasticity material type 24 (MAT_024) is an elasto-plastic material in which an arbitrary stress–strain curve and arbitrary strain-rate dependency can be defined. In addition, failure based on plastic strain or a minimum time step size can be defined.

Crushable-foam material type 63 (MAT_063) is dedicated to modeling crushable foam with optional damping and tension cutoff. Unloading is fully elastic. Tension is treated as elastic-perfectly-plastic at the tension cutoff value.

Table A1. Material mechanical property parameters of the battery pack components.

Component	MAT_ID	Rio (g/cm^3)	E (MPa)	PR	YS (MPa)	TS (MPa)
Foam	MAT_001	0.045	1	0.45	-	-
Indenter	MAT_020	7.850	210,000	0.3	-	-
Bottom supports	MAT_020	7.850	210,000	0.3	-	-
Ball-punch	MAT_020		210,000	0.3		
Cell shell	MAT_024	2.700	70,000	0.33	95	140
PVC	MAT_024	1.300	3000	0.35	10	60
Jellyroll	MAT_063	2.377	2700	0.01	-	-

References

1. Wang, S.J. Analysis of electric vehicle fire accidents and exploration of fire protection measures. *Fire Sci. Technol.* **2024**, *43*, 1037–1042.
2. Xia, Y.; Wierzbicki, T.; Sahraei, E.; Zhang, X. Damage of cells and battery packs due to ground impact. *J. Power Sources* **2014**, *267*, 78–97. [CrossRef]
3. Rawlinson, P.; Clarke, A.; Gadhiya, H. System for Absorbing and Distributing Side Impact Energy Utilizing an Integrated Battery Pack. U.S. Patent US201816034738A, 22 September 2020.
4. Zhu, J.; Zhang, X.; Wierzbicki, T.; Xia, Y.; Chen, G. Structural designs for electric vehicle battery pack against ground impact. In Proceedings of the WCX World Congress Experience, Detroit, MI, USA, 10–12 April 2018.
5. Zhang, S.; Zhou, Q.; Xia, Y. Influence of mass distribution of battery and occupant on crash response of small lightweight electric vehicle. *SAE Tech. Pap.* **2015**. [CrossRef]
6. Xia, Y.; Chen, G.; Zhou, Q. Failure behaviours of 100% SOC lithium-ion battery modules under different impact loading conditions. *Eng. Fail. Anal.* **2017**, *82*, 149–160. [CrossRef]
7. Kukreja, J.; Nguyen, T.; Siegmund, T. Crash analysis of a conceptual electric vehicle with a damage tolerant battery pack. *Extreme Mech. Lett.* **2016**, *9*, 371–378. [CrossRef]
8. Wang, H.; Kumar, A.; Simunovic, S.; Allu, S.; Kalnaus, S.; Turner, J.A.; Helmers, J.C.; Rules, E.T.; Winchester, C.S.; Gorney, P. Progressive mechanical indentation of large-format Li-ion cells. *J. Power Sources* **2017**, *341*, 156–164. [CrossRef]
9. Soudbakhsh, D.; Gilaki, M.; Lynch, W.; Zhang, P.; Choi, T.; Sahraei, E. Electrical Response of Mechanically Damaged Lithium-Ion Batteries. *Energies* **2020**, *13*, 4284. [CrossRef]
10. Sahraei, E.; Bosco, E.; Dixon, B. Microscale failure mechanisms leading to internal short circuit in Li-ion batteries under complex loading scenarios. *J. Power Sources* **2016**, *319*, 56–65. [CrossRef]
11. Forbes, G.; Robinson, J. *The Safety Impact of Vehicle-Related Road Debris*; Crash Rates; AAA Foundation for Traffic Safety: Washington, DC, USA, 2004.
12. Sormunen, O.V.E.; Kõrgesaar, M.; Tabri, K. Comparing rock shape models in grounding damage modelling. *Mar. Struct.* **2016**, *50*, 205–223. [CrossRef]
13. Chung, S.H.; Tancogne-Dejean, T.; Zhu, J.; Luo, H.; Wierzbicki, T. Failure in lithium-ion batteries under transverse indentation loading. *J. Power Sources* **2018**, *389*, 148–159. [CrossRef]
14. Wang, H.; Simunovic, S.; Maleki, H.; Howard, J.N.; Hallmark, J.A. Internal configuration of prismatic lithium-ion cells at the onset of mechanically induced short circuit. *J. Power Sources* **2016**, *306*, 424–430. [CrossRef]
15. Marcicki, J.; Bartlett, A.; Yang, X.G.; Mejia, V.; Zhu, M.; Chen, Y. Battery Abuse Case Study Analysis Using LS-DYNA. In Proceedings of the 14th International LS-DYNA Users Conference, Dearborn, MI, USA, 12–14 June 2016.
16. Zhang, X.; Sahraei, E.; Wang, K. Li-ion Battery Separators, Mechanical Integrity and Failure Mechanisms Leading to Soft and Hard Internal Shorts. *Sci. Rep.* **2016**, *6*, 32578. [CrossRef] [PubMed]
17. Sahraei, E.; Hill, R.; Wierzbicki, T. Calibration and finite element simulation of pouch lithium-ion batteries for mechanical integrity. *J. Power Sources* **2012**, *201*, 307–321. [CrossRef]
18. Logakannan, K.P.; Zhu, F.; Sypeck, D.; Deng, J.; Kim, S. Dynamic Indentation of Prismatic Li-Ion Battery Cells. In *Dynamic Behavior of Soft and Hard Materials Volume 1*; IMPLAST 2022; Springer Proceedings in Materials; Springer: Singapore, 2024; Volume 34.
19. Kisters, T.; Gilaki, M.; Nau, S.; Sahraei, E. Modeling of Dynamic Mechanical Response of Li-Ion cells with Homogenized Electrolyte-Solid Interactions. *J. Energy Storage* **2022**, *49*, 104069. [CrossRef]

20. Pan, Z.; Li, W.; Xia, Y. Experiments and 3D detailed modeling for a pouch battery cell under impact loading. *J. Energy Storage* **2020**, *27*, 101016. [CrossRef]
21. Bulla, M.; Kolling, S.; Sahraei, E. A material model for the orthotropic and viscous behavior of separators in lithium-ion batteries under high mechanical loads. *Energies* **2021**, *14*, 4585. [CrossRef]

Disclaimer/Publisher's Note: The statements, opinions and data contained in all publications are solely those of the individual author(s) and contributor(s) and not of MDPI and/or the editor(s). MDPI and/or the editor(s) disclaim responsibility for any injury to people or property resulting from any ideas, methods, instructions or products referred to in the content.